Bragg grating based nanophotonic biochemical sensor with enhanced light matter interaction

M. A. IBRAR JAHAN[1,*], VENKATESHA MUNISWAMY[2], CIRO RODRIGUEZ[3], RAJINI V. HONNUNGAR[1]
[1]*Department of Electronics and Communication Engineering, RNS Institute of Technology, VTU, Bengaluru, India*
[2]*Department of Electronics and Communication Engineering, SaiVidya Institute of Technology, VTU, Bengaluru, India*
[3]*Department of Software Engineering, Universidad Nacional Mayor de San Marcos University Lima, Peru*

A silicon-based nanophotonic device with increased light-matter interaction is presented for biochemical sensing. This article describes the design of an SOI-based rib waveguide with gratings. Using the Finite-Difference Time-Domain (FDTD) Lumerical tool, a numerical analysis is done to evaluate the sensing capabilities of the proposed photonic biochemical sensor. A gold layer is sandwiched between the upper and lower SiO_2 layers. Gratings and the gold reflector layer below the waveguide have increased light-matter interaction resulting in enhanced sensitivity. The sensor is tailored for a 1550 nm operating wavelength. Achieved a high sensitivity of 1160 nm/RIU with a Full Width Half Maxima (FWHM) of 6.8 nm and a Figure of Merit (FOM) of 171/RIU. The proposed sensor has a high sensitivity making it a viable option for various biochemical sensing applications, so the designed sensor is used in the detection of malaria disease.

1. Introduction

Optical biosensors are sensor devices that employ optical principles to convert a biological interaction into an appropriate output signal. Optical biosensing technology can be used in place of standard analytical techniques since it eliminates the need for costly, difficult, and time-consuming detection procedures. Optical sensing has several advantages over electrical sensing, including the lack of electrical shocks or explosions, resilience to electromagnetic interference, and, in general, higher sensitivity and broader bandwidth. Additionally, remote sensing is feasible via the use of optical fibers to steer light toward and away from the device [1]. All of these features make them an attractive alternative to established medical diagnostic and biomolecular sensing techniques. Optical biosensors are classified as labeled and unlabeled biosensors. Label-based sensing involves the labeling of target molecules with fluorescent markers that can detect the presence of the desired biomolecule. Not only is this technique time consuming and costly, but it is also more sophisticated and requires specialized employees for labeling and measuring. The label-free solutions do not necessitate the use of labels/markers. This sensing technology makes use of a bio-receptor to ensure that the target molecule binds to the sensing surface via electrostatic interaction or a variety of secondary interactions. Typically, the surface is a waveguide or optical sensing element [2]. Label-free biosensors based on the refractive index (RI) have increasingly gained interest in recent years due to the simplicity of their measurement process. When the target molecule adheres to the waveguide sensor structure, the refractive index of

the peripheral layer alters, significantly changing the propagation characteristics of the optical signal [3]. To accomplish label-free detection, the modification in characteristics is quantified. Numerous RI-based sensors have been investigated for biosensing, with planar waveguides, Bragg gratings, slot, dual slot, strip waveguides, ring resonators, and interferometers serving as the optical sensing element [4-10].

Waveguide Biosensors based on Bragg gratings detect a wavelength shift in the Bragg wavelength caused by a change in the RI at the grating surface. Such sensors can be used for multiplexed sensing and have the capability for lab-on-chip integration [11-13]. One critical issue to design waveguide Bragg grating based sensors is, that the waveguide should satisfy single mode conditions so that leaky modes due to mode coupling can be avoided [14]. This requires shrinking the dimensions of waveguide Bragg grating based sensors with the slot or strip waveguide sub-micron range. This constraint can be circumvented by adopting a rib waveguide, which enables single mode operation while retaining larger dimensions, by selecting a suitable ratio of the waveguide's dimensions. Bragg gratings offer advantages like smaller silicon footprints and reduced bending losses [15].

The work presented in this article is an extension of the work that is previously reported in [16]. A nanophotonic grating in a rib-based silicon waveguide that can be used for biochemical sensing is designed with the help of a Silicon-on-Insulator (SOI) substrate. The silicon gratings have a grating period Λ that is less than the resonating wavelength and they are arranged in a periodic pattern in the direction of the incoming light. The numerical investigation focuses on determining how the

optical characteristics of the sensor are affected by the geometrical factors. It is possible to change the effective index of the medium by adjusting the rib width, etch depth, grating period and duty cycle. Between the top and bottom SiO₂ layers, a 40 nm thick gold layer is deposited to increase the light's confinement to the core and thus the time of light-matter interaction [17-20]. The sensor is found to have a sensitivity of 1160 nm/RIU with an FWHM of 6.8 nm and FOM of 171/RIU. The optimized device is used for the diagnosis of malaria disease in the blood. The sensor has a footprint area of 12.25 μm^2 and can be used in biosensing applications.

2. Sensor design

The proposed sensor consists of Bragg gratings on a rib waveguide designed on the SOI platform. Fig. 1(a) shows the schematic of the sensor, a gold layer is deposited between the top and bottom SiO₂ layer. The light is propagating through the x-direction. Fig. 1(b) shows a side view of the device. Λ is the grating period, H is the total height of the device and d is the etch depth.
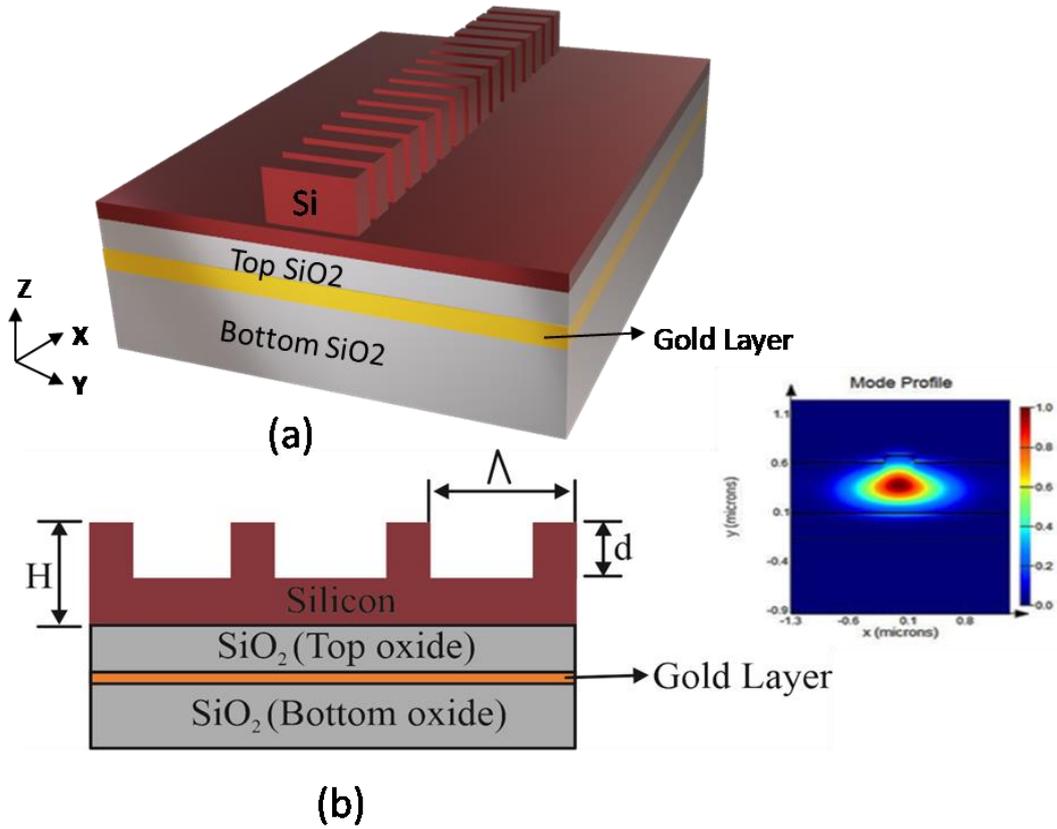

Fig. 1. (a) Rib waveguide with gratings is depicted schematically supporting single mode.
(b) Side view of the device (color online)

When the light propagates through the gratings part of the light is transmitted and the remaining light is reflected. According to Bragg's condition, Bragg's wavelength is expressed in Eq. 1.

$$\lambda_B = 2 n_{eff} \Lambda \qquad (1)$$

Λ is the grating period, n_{eff} is an effective index and λ_B is Bragg's wavelength. The spectral response of the grating device can be customized by modulating the gratings etch depth, width and grating period. The gratings created on the silicon rib must have a small grating period than Bragg's condition $\Lambda \ll \lambda/(2n_{eff})$ so a grating period of 280 nm is selected as the operating wavelength

of 1550 nm and n_{eff} is 2.77. The height of the waveguide (H) is 280 nm and a rib width of 500 nm is selected. The gratings over the rib induce resonance in the device. One of gold's unusual characteristics is the ability to reflect light [21], which helps to provide strong optical confinement. To increase the device sensitivity and to prevent optical field leakage through the bottom SiO₂ layer, a gold layer of 40 nm is deposited between the top and bottom SiO₂ layers. With the inclusion of the gold layer, the total height of the device is 320 nm. To achieve high sensitivity, the grating depth, rib width and grating period are all fine-tuned. The maximum optical field is confined within the silicon/air gratings, which causes the device to resonate. This, in turn, increases the time of interaction of the light and the analyte which ultimately results in the device's increased sensitivity. When a

numerical simulation is performed, the upper cladding layer is assumed to be the analyte. A numerical study of the device is carried out with the aid of Lumerical simulation tools such as MODE profile and 3D Finite-Difference Time-Domain (FDTD), which produces accurate quantitative data. These simulators can be utilized to acquire an understanding of the device characteristics and properties [22]. During the simulation, a wavelength of 1550 nm is considered, and the mesh resolution is set to auto non-uniform. A Perfectly Matched Layer (PML) is employed so that outgoing waves can be absorbed to prevent back reflections into the active area. Table 1 presents the proposed sensor specifications.

Table 1. Sensor Specifications

Sl. No.	Design Specifications	Dimensions (nm)
1	Rib width (W)	500
2	Slab height (h)	220
3	Height of the waveguide (H)	280
4	Grating depth (d)	60
5	Gold layer Thickness	40
6	Operating wavelength (λ)	1550
7	Grating Period (Λ)	280
8	Duty cycle (DC)	50 %

3. Sensor performance characteristics

On the silicon rib, periodic gratings are etched to achieve strong optical field confinement. When the cladding's refractive index is altered, a large shift in the wavelength occurs, enhancing the device's sensitivity. Narrower FWHM is another parameter that is desirable for a notable shift in wavelength. In sensing devices, the figure of merit (FOM) and sensitivity (S) are used to determine the sensor's performance [23]. Bulk sensitivity is expressed as the measure of wavelength shift per unit change in the refractive index of the analyte as given by Eq. 2.

$$S = \frac{\Delta\lambda_B}{\Delta n_c} \quad (2)$$

where $\Delta\lambda_B$ is the change in Bragg's/resonance wavelength, Δn_c is a change in the refractive index of the analyte and S is the sensitivity.

The figure of merit (FOM) is given by the ratio of the sensitivity of the device to the full width half maxima (FWHM) as shown in Eq. 3.

$$FOM = \frac{S}{FWHM} \quad (3)$$

Changing the gold layer thickness, grating period and keeping constant the depth of the grating and the width of the rib allows us to numerically observe the influence on the performance of the device. The analyte considered is

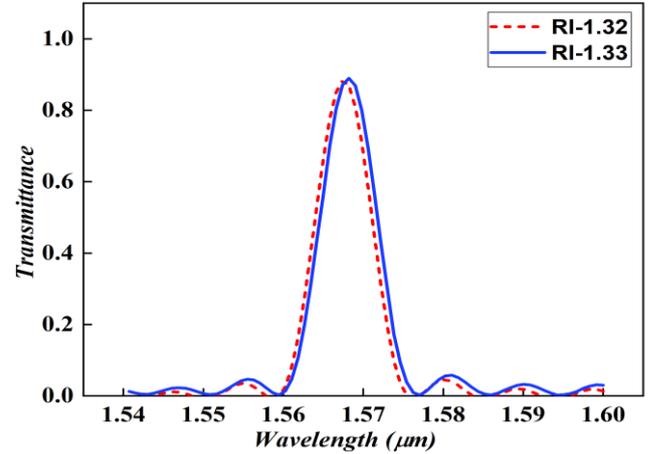water and ethanol with a refractive index of 1.32 and 1.33 [24].

Fig. 2. Transmittance plot with RI 1.32 and 1.33 (color online)

Fig. 2 shows the transmittance curve obtained with a gold layer of 40 nm deposited between the bottom and top SiO$_2$ layer. The duty cycle is defined as the ratio of the width of the grating rib with the grating period. DC is set at 50% for maximum coupling efficiency. A grating period of 280 nm, rib width of 500 nm and grating depth of 60 nm is considered. The refractive index of the analyte is changed from 1.32 to 1.33. TE polarization is considered since the shift in wavelength is more. When the analyte refractive index is changed Bragg's wavelength is shifted and the sensitivity is calculated. Achieved a bulk sensitivity of 1160 nm/RIU, FWHM of 6.8 nm and FOM of 171/RIU. As per Bragg's law as the grating period increases the resonant wavelength must also increase as shown in Fig. 3. The grating period is varied between 280 nm to 320 nm with a rib width of 500 nm, a grating depth of 60 nm, and a gold layer of 40 nm. The duty cycle is set at 50%
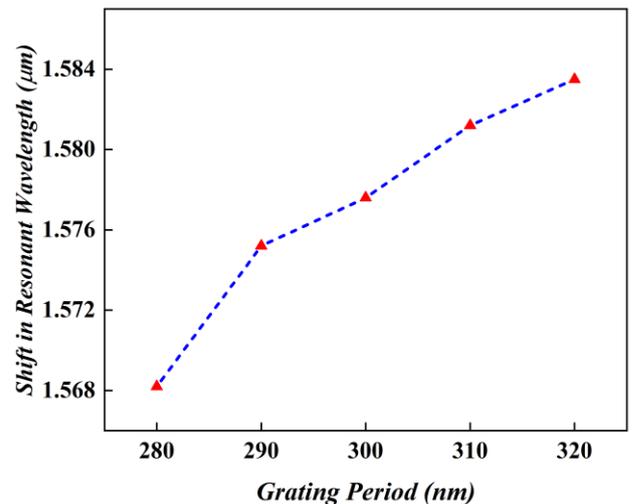

Fig. 3. Wavelength shift vs grating period (color online)

Due to the gold's light reflecting property strong optical confinement in the active area (Si rib and gratings) is possible to achieve. By varying the thickness of the gold layer, the sensor performance is evaluated further. The thickness of the gold layer is increased from 20 nm to 50 nm by maintaining the width at 500 nm, the grating depth at 60 nm and the grating period at 280 nm. With an increase in gold layer thickness, a considerable shift in wavelength is observed and the more the wavelength shifts higher the sensitivity. At 50 nm gold layer thickness, the wavelength shift is negligible as shown in Fig. 4.
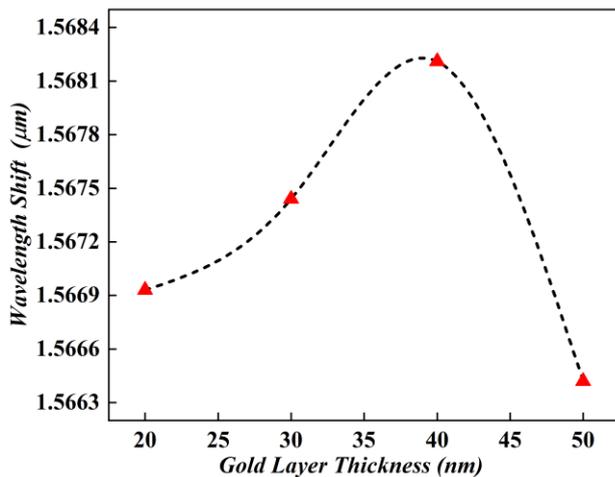

Fig. 4. Wavelength shift vs gold layer thickness (color online)

Since sensitivity is dependent on wavelength shift, a 40 nm gold layer thickness has been considered. The analyte is placed into the cladding region and the optical confinement factor which estimates the proportion of mode complex power that flows through a waveguide's cross-section and is given by Eq. 4.

$$\Gamma_C = \frac{\iint_c |E(x,y)|^2 dx\, dy}{\iint_\infty |E(x,y)|^2 dx\, dy} \qquad (4)$$

With the aid of the Mode solver tool obtained a value of 70% for the optical field confinement factor [13]. In our previous work it was concluded that such a type of biosensor may be used in biochemical sensing to identify diseases and the biosensor that is optimized in this work has a high sensitivity in comparison to the work that we have previously reported. So to diagnose malaria disease, the optimized sensor is used.

4. Proposed sensor for detection of diseases

4.1. Detection of malaria disease

Malaria is the leading disease and death across the globe, affecting around 500 million people with febrile episodes and hundreds of thousands of deaths per year are caused by a mosquito-borne illness that primarily affects humans and other animals. It typically spreads via a mosquito Anopheles that is infected. The mosquito introduces the parasites from its saliva into the human bloodstream. These parasites go to the liver and begin to reproduce [25-26]. During asexual development, the three stages of structural change that occur in the RBC are commonly identified:

1. A ring stage with ring-like characteristics that persist for a total of 24 hours
2. The trophozoid stage occurs during the 24- to 36-hour
3. The schizont stage during the 36–48 hours

An infected red blood cell has a non-homogeneous refractive index distribution whereas a normal red blood cell has homogeneous distribution in refractive index. Thus, there is a significant difference in refractive index between infected and healthy red blood cells (RBC). This parameter can be used for the diagnosis of malaria disease [27]. Table 2 shows the refractive index of the normal and infected red blood cells.

Table 2. Refractive index values for normal and infected red blood cells in malaria disease [27]

Types of cell	Refractive Index
Normal red blood cell	1.402
Ring stage-infected cell	1.395
Trophozoites stage-infected cell	1.383
Schizont stage-infected cell	1.373

The plot of the wavelength shift for the analyte's refractive index, which ranges from 1.373 to 1.402 can be shown in Fig. 5. It has been found that the shift in wavelength is around 1.5664 µm when the RI value is 1.373 and an even greater shift in wavelength can be observed when the RI value is 1.402.
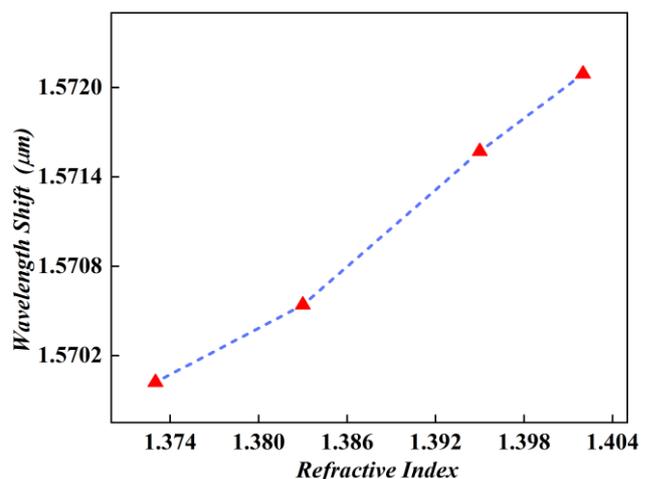

Fig. 5. Wavelength shift vs refractive index change (color online)

Fig. 6 depicts the sensor's transmission spectrum in the presence of an analyte with a refractive index ranging from 1.373 to 1.402 for healthy and infected red blood cells, respectively. As the analyte varies, the effective refractive index of the device also changes, resulting in a shift in wavelength owing to a fluctuation in the reflective power.
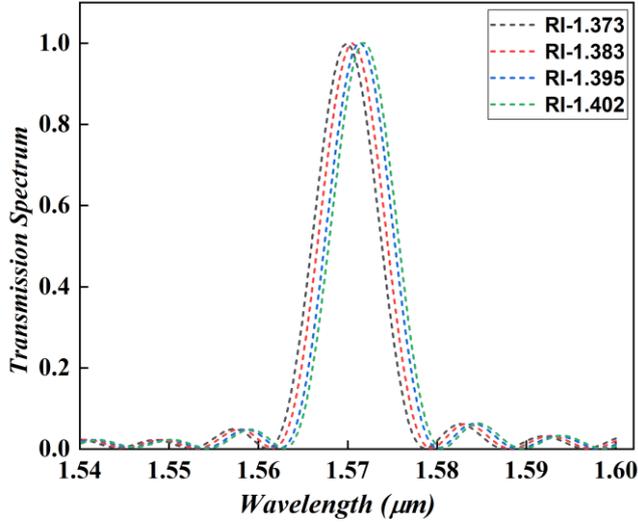
due to their small footprint. Obtained a Q factor of 231, the sensor provides stable thermal behavior due to its low Q factor. By optimizing device dimensions and choosing an operating wavelength of 1310 nm, the Q factor can be enhanced, as water-based analyte losses are reduced at this wavelength [31-32].

Fig. 6. Transmission spectrum of refractive index ranging from 1.373 to 1.402 (color online)

It is obvious from the preceding discussion that high sensitivity is a significant design criterion for a sensor with high sensitivity. In terms of sensitivity, footprint area and analyte to be detected, Table 3 compares the proposed study to previously published research. The proposed sensor has a sensitivity of 1160 nm/RIU, a footprint area of 12.25 μm^2, with a narrow FWHM of 6.8 nm. The nanophotonic grating device that has been proposed provides an improvement that is 2.339 times more than the claimed sensitivity of a sensor that is based on a photonic crystal [23], 3.2954 times the sensitivity of cavity based grating sensor [28], 3.1955 times the sensitivity of subwavelength grating based micro ring resonator [29], 2.7039 times the sensitivity of SWG based race track resonator [9] and is closer to the sensitivity of the grating based slot waveguide reported in [13]. The sensor's footprint area which is its dimension is 12.25 μm^2 in comparison to 80 μm^2 reported in subwavelength grating-based micro-ring sensors [29]. Batch processing of such devices utilizing CMOS-compatible technology is feasible

Table 3. Comparison of previously reported work

Type of Device	Sensitivity	Foot Print Area (μm^2)	Sensing Analyte
Photonic Crystal [23]	495.73 nm/RIU	11.5	RBC in blood
Grating structure with cavity [28]	352 nm/RIU	18	NaCl
Subwavelength grating-based micro-ring [29]	363 nm/RIU	80	Glucose
SWG racetrack resonator [9]	429 nm/RIU	-	DI water
Grating based slot waveguide [13]	1200 nm/RIU	-	HBsAg
Proposed Sensor	1160 nm/RIU	12.25	RBC in blood

5. Fabrication Process flow steps of the proposed Sensor

Fig. 7 exhibits the simulation of the fabrication process flow steps of the SOI waveguide structure using Intellisense software (Lynnfield, MA, USA) [30].
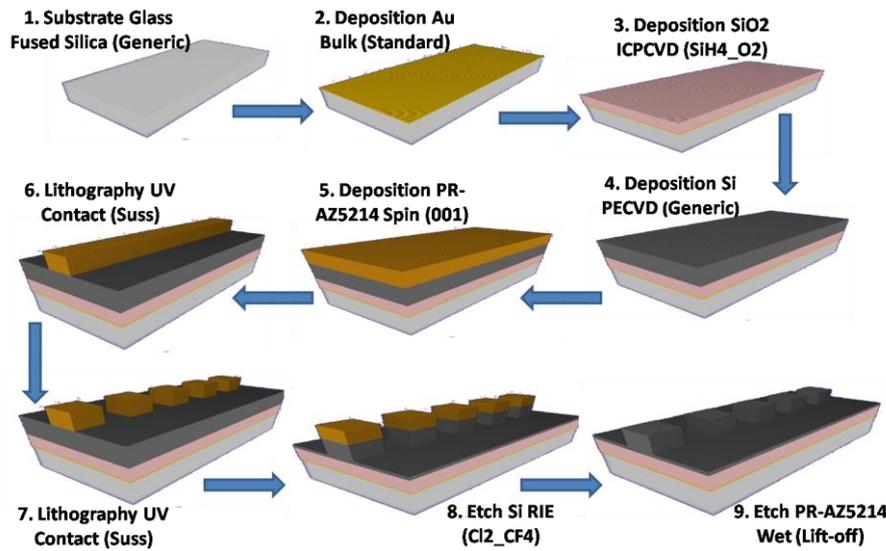
Fig. 7. Process flow steps for the proposed SOI waveguide based sensor (color online)

The following steps show the flow of the fabrication process:

i. The substrate is glass (Fused Silica), thickness of the fused silica (Glass) wafer is 2 μm.

ii. Deposition of gold Au (Standard) of thickness 40 nm (conformal)

iii. Deposition of SiO_2 of 250 nm thickness using the ICPCVD (SiH4_O2)

iv. Deposition of Si of 220 nm thickness using PECVD (Generic)

v. Deposition of PR-AZ5214 of 300 nm thickness using Spin coating

vi. Lithography Layer 1(GDS#1): Leave Photoresist Inside using UV Contact (Suss)

vii. Lithography Layer 2(GDS#2): Leave Photoresist Inside using UV Contact (Suss)

viii. Etch Si RIE (Cl2_CF4): Etch Thickness: 310 nm (Partial Etch)

iX. Etch PR-AZ5214 Wet (Lift-off): Etch Thickness: Lift off

X. Etch PR-AZ5214 Wet (Lift-off): Etch Thickness: Lift off

6. Conclusion

The performance study of bulk sensing in tailored Bragg gratings based waveguide structure is proposed. The device has been designed using a comprehensive procedure: first, the structure is dimensioned to optimize the device sensitivity and then to further enhance the sensitivity, a gold layer is sandwiched between the top and bottom SiO_2 layer. A sensitivity of 1160 nm/RIU, FWHM of 6.8 nm and FOM of 171/RIU is achieved. In comparison to previously designed sensors, the device exhibits exceptional features like enhanced optical confinement, a tenfold increment in sensitivity and a narrow FWHM. These findings will pave the way for the future application of this new concept in photonic structures for on-chip biochemical sensing.

References

[1] J. Walter, A. Eilers, L. Shanika, M. Alwis, B. W. Roth, K. Bremer, Sensors **20**, 1 (2020).
[2] S. Sang, Y. Wang, Q. Feng, Y. Wei, J. Ji, W. Zhang, Crit. Rev. Biotechnol. **36**, 465 (2016).
[3] Ye Fang, Drug Discov Today Technol. **7**, e5 (2010).
[4] E. Luan, H. Shoman, D. M. Ratner, K. C. Cheung, L. Chrostowsk, Sensors **18**, 1 (2018).
[5] L. M. Lechuga, Chapter 5 Optical Biosensors, Comprehensive Analytical Chemistry **44**, 209 (2005).
[6] R. Soref, IEEE J. Sel. Top. Quantum Electron. **12**, 1678 (2006).
[7] R. Mejard, H. J. Griesser, B. Thierry, TrAC - Trends Anal. Chem. **53**, 178 (2014).
[8] W. C. Lai, S. Chakravarty, Y. Zou, Y. Guo, R. T. Chen, Appl. Phys. Lett. **102**, 1 (2013).
[9] Lijun Huang, Hai Yan, Xiaochuan Xu, Swapnajit Chakravarty, Naimei Tang, Huiping Tian, Ray T. Chen, Opt. Express **25**, 10527 (2017).
[10] L. Zhang, D. Dai, IEEE Photonics Technol. Lett. **31**, 1209 (2019).

[11] Xiaoguang Tu, Junfeng Song, Tsung-Yang Liow, Mi Kyoung Park, Jessie Quah Yiying, Jack Sheng Kee, Mingbin Yu, Guo-Qiang Lo, Opt. Express **20**, 2640 (2012).

[12] Sulabh, Vishal Kaushik, Lalit Singh, Swati Rajput, Mukesh Kumar, J. Opt. Soc. Am. B. **38**, 749 (2021).

[13] Sulabh, L. Singh, S. Jain, M. Kumar, IEEE Sens. J. **19**, 6126 (2019).

[14] X. Wang, W. Shi, S. Grist, H. Yun, N. A. F. Jaeger, L. Chrostowski, IEEE Photonic Soc. 24th Annu. Meet. **19**, 869 (2011).

[15] Y. S. Hong, C. H. Cho, H. K. Sung, Sensors **18**, 1 (2018).

[16] I. J. Aslam, V. Muniswamy, L. Singh, M. Sathish, R. V. Honnungar, Silicon **54**, 1 (2022).

[17] V. M. N. Passaro, R. Loiacono, G. D'Amico, F. De Leonardis, IEEE Sens. J. **8**, 1603 (2008).

[18] Seong Phun Chana, Vittorio M. N. Passaro, S. T. Lima, C. E. Pnga, W. Headleya, G. Masanovica, Graham T. Reeda, R. M. H. Attac, G. Ensellc, A. G. R. Evansc, Semicond. Optoelectron. Devices Light. Communication **5248**, 273 (2003).

[19] A. S. Jugessur, J. Dou, J. S. Aitchison, R. M. De La Rue, M. Gnan, Microelectron. Eng. **86**, 1488 (2009).

[20] Y. Ishizaka, S. Makino, T. Fujisawa, K. Saitoh, IEEE Photonics J. **9**, 1 (2017).

[21] V. M. N. Passaro, F. Dell'Olio, C. Ciminelli, M. N. Armenise, Sensors **9**, 1012 (2009).

[22] J. Ctyroky, P. Kwiecien, J. Wang, I. Richter, I. Glesk, L. Chen, Integr. Opt. Phys. Simulations II. **9516**, 95160M1 (2015).

[23] U. Biswas, J. K. Rakshit, Opt. Quantum Electron. **52**, 1 (2020).

[24] S. Heinsalu, Y. Isogai, Y. Matsushima, H. Ishikawa, K. Utaka, Optics Express **28**, 28126 (2020).

[25] V. Sharma, V. L. Kalyani, Int. J. Emerg. Res. Manag. Technol. **6**, 1 (2018).

[26] Ankita Goyal, B. Suthar, A. Bhargava, Plasmonics **16**, 59 (2021).

[27] S. Bendib, C. Bendib, J. Biosens. Bioelectron. **9**, 1 (2018).

[28] Sourabh Jain, Sulabh, Swati Rajput, Lalit Singh, Pragya Tiwari, Arvind Shrivastava, Mukesh Kumar, IEEE Sens. J. **20**, 3529 (2020).

[29] Z. Tu, D. Gao, M. Zhang, D. Zhang, Opt. Express **25**, 20911 (2017).

[30] V. Muniswamy, C. Muniraju, Kumar P. Pattnaik, N. Krishnaswamy, Micromachines **9**, 134 (2018).

[31] U. Biswas, J. K. Rakshit, G. K. Bharti, Opt. Quant. Electron. **52**, 1 (2020).

[32] R. Kaur, G. Kumar Bharti, A. Tripathi, 2022 2nd Asian Conference on Innovation in Technology (ASIANCON) 1-4 (2022).

*Corresponding author: ibrarjahan.ec@gmail.com